

**ROSAT X-RAY OBSERVATIONS OF
THE RADIO GALAXY NGC 1316 (FORNAX A)**

D.-W. Kim

*Chungnam National University, Taejon, 305-764, South Korea; and
Harvard-Smithsonian Center for Astrophysics, 60 Garden Street, Cambridge, MA 02138*

G. Fabbiano and G. Mackie¹

Harvard-Smithsonian Center for Astrophysics, 60 Garden Street, Cambridge, MA 02138

June 26, 2021

1. Visiting Astronomer, Cerro Tololo Inter-American Observatory.

Abstract

We have observed NGC 1316 (Fornax A) with the ROSAT HRI. In this paper, we present the results of these observations and we complement them with the spectral analysis of the archival PSPC data. The spectral properties suggest the presence of a significant component of thermal X-ray emission ($> 60\%$), amounting to $\sim 10^9 M_\odot$ of hot ISM. Within $3'$ from the nucleus of NGC 1316, the HRI X-ray surface brightness falls as r^{-2} . In the inner $\sim 40''$, the X-ray surface brightness is significantly elongated ($\epsilon \sim 0.3$). This flattened X-ray feature is confirmed by a straightforward statistics test as well as moment analysis. By comparing the morphology of the X-ray emission with the distribution of optical dust patches, we find that the X-ray emission is significantly reduced at the locations where the dust patches are more pronounced, indicating that at least some of the X-ray photons are absorbed by the cold ISM. We also compare the distribution of the hot and cold ISM with that of the ionized gas, using recently obtained H_α CCD data. We find that the ionized gas is distributed roughly along the dust patches and follows the large scale X-ray distribution at $r > 1'$ from the nucleus. However, there is no one-to-one correspondence between ionized gas and hot gas. Both morphological relations and kinematics suggest different origins for hot and cold ISM. The radio jets in projection appear to pass perpendicularly through the central X-ray ellipsoid. Comparison of thermal and radio pressures suggests that the radio jets are confined by the surrounding hot gaseous medium.

1. INTRODUCTION

NGC 1316 (Fornax A, Arp 154) is a giant elliptical galaxy in the poor Fornax cluster. This galaxy exhibits many unusual features for an elliptical galaxy, including pronounced dust patches, H_α filaments, ripples and loops (e.g., Arp 1966; Schweizer 1980; Carter et al. 1983; Mackie and Fabbiano 1997). The distribution of the optical surface brightness reveals an extensive envelope, making NGC 1316 a typical D (or cD) galaxy (Schweizer 1980). It has one of the most pronounced shell systems observed in early type galaxies (Malin and Carter 1983). These features all point to a recent merging in NGC 1316 (e.g., Schweizer 1980).

In the radio (0.03 - 5 GHz), Fornax A is one of the brightest objects in the sky ($L = 2 \times 10^{42}$ erg sec $^{-1}$; Ekers et al. 1983). It contains giant radio lobes (Wade 1961), separated by $\sim 30'$ (~ 240 kpc), consisting of polarized, organized filaments (Fomalont et al. 1989). A faint bridge between the lobes is displaced to the south of the galaxy center and S-shaped nuclear radio jets are present, implying a significantly violent action in the galaxy history, as also suggested by the optical data (e.g., Ekers et al. 1983; Geldzahler and Fomalont 1984). The nucleus of NGC 1316 hosts a low-luminosity AGN: optically it has a LINER-type spectrum (Veron-Cetti and Veron 1986; Baum, Heckman and van Breugel 1992); it contains a radio core (Geldzahler and Fomalont 1984); and HST observations have revealed a nuclear UV-bright point source (Fabbiano, Fassnacht and Trinchieri 1994b). NGC 1316 also contains complex, multiphase ISM: it has been detected in optical emission lines from ionized gas (e.g., Schweizer 1980; Phillips et al. 1986; Veron-Cetti and Veron 1986), IRAS far infrared emission (Knapp et al. 1989) and CO lines of molecular gas (Wiklind and Henkel 1989; Sage and Galletta 1993).

In X-rays, NGC 1316 was detected with Einstein (Fabbiano, Kim and Trinchieri 1992) and belongs to a group with the lowest L_X/L_B ratio among E and S0 galaxies (Kim, Fabbiano and Trinchieri 1992b). Therefore, based on the global amount of X-ray emission, NGC 1316 does not necessarily contain a large amount of hot ISM (see Fabbiano, Gioia and Trinchieri 1988). In this, it is similar to other galaxies which may have experienced recent mergers (Hibbard et al. 1994; Fabbiano and Schweizer 1995). ROSAT PSPC (Feigelson et al. 1995) and ASCA observations (Kaneda et al. 1995) have revealed the presence of extended Inverse Compton X-ray emission at the locations of radio lobes.

In this paper, we discuss the results of a re-analysis of the archival ROSAT (Truemper 1983) PSPC observation of NGC 1316, and we report for the first time the results of high

resolution X-ray observation with the ROSAT HRI. The HRI has ~ 5 arcsec resolution (David et al 1993), comparable to that of ground-based radio and optical data. With these data we establish the presence of a hot ISM in NGC 1316 and we correlate its properties to that of the other phases of the ISM. We also explore possible interactions between this hot ISM and the active radio nucleus.

This paper is structured as follows: in section 2, we present the results of the ROSAT HRI (§2.1 and §2.2) and the ROSAT PSPC data analysis (§2.3); in section 3, we compare the X-ray data with the optical and radio data; finally, in section 4 we discuss the implications of our results.

2. X-RAY OBSERVATIONS

NGC 1316 was observed with the ROSAT HRI on Jan. 14, 1994 and Jul. 7-10, 1994 for a total exposure time ~ 40 ks (3/4 of total observations were obtained in the July run). The two data sets are consistent with each other within the observational uncertainty. We present the combined results except as mentioned in §2.1. The field of view of this observation also includes the companion elliptical galaxy NGC 1317 (Figure 1). The observational log and basic parameters of both galaxies are given in Table 1. NGC 1316 was also observed with the ROSAT PSPC (Feigelson et al. 1995), and we used the PSPC archival data to determine spectral parameters.

Given the limited statistics of our HRI observation, we have used various binning and smoothing factors to investigate both large scale (a few arcmin) and small scale ($\lesssim 1$ arcmin) features. We used both IRAF and software we developed ourselves to analyze our data. We adopt a distance to NGC 1316 of 27.2 Mpc using $H_o = 50 \text{ km s}^{-1} \text{ Mpc}^{-1}$ (Fabbiano et al. 1992).

To extract source data, the field background must be subtracted. We found that estimates from the background map generated by the standard ROSAT SASS processing and from local measures of the background in concentric annuli around the sources agree well with each other. We will present results obtained with the local background subtraction.

2.1 X-ray Emission Features and Sources

The entire observed field of view is shown in Figure 1, where the X-ray contour map is overlaid on the optical image obtained from the Digitized Optical Survey⁽²⁾. The X-ray

image was binned with a pixel size of $8''$ and smoothed with a Gaussian of $\sigma = 16''$. The background is not subtracted. The octagonal shape indicates the boundary of the HRI detector. The figure shows a strong X-ray source at the center of the field, corresponding to the optical position of NGC 1316. Also X-ray emission is detected at the optical position of NGC 1317 ($6.3''$ to north of NGC 1316). Additionally, 10 point-like sources (above 3σ) are detected in the observed field. The source position, radius of the count extraction circle and X-ray count for each source are listed in order of RA in Table 2. The corresponding source numbers are marked in Figure 1. X-ray counts were extracted from circular regions centered on their X-ray centroids. The radius was determined with the radial profile of the X-ray surface brightness (§2.2). Typically these radii extend to where the surface brightness is within $\sim 3-4\%$ of the background. The background counts were extracted in annuli $r=60'' - 200''$, except for NGC 1316 where an annulus $r=200'' - 400''$ is used.

2. The Digitized Sky Survey was produced at the Space Telescope Science Institute under U.S. Government grant NAG W-2166. The images of these surveys are based on photographic data obtained using the Oschin Schmidt Telescope on Palomar Mountain and the UK Schmidt Telescope.

With the HRI observation of NGC 1316 we can trace the X-ray emission out to $170''$, or 22.4 kpc at an adopted distance of 27.2 Mpc (see §2.2). However, the X-ray emission is extended at least to $1000''$ (Fabbiano et al. 1992; Feigelson et al. 1995). The other sources (including NGC 1317) are point-like. Except for NGC 1316 and 1317, the sources are not identified with known objects in the SIMBAD catalog.

Source 2 and 12 are possibly variable. Their count rates from the two HRI observing epochs (Table 1) are significantly different (above 3σ), while count rates of other sources are consistent within the count errors between the two observations (see Table 3). The small numbers of source counts do not warrant further temporal analysis.

The number of serendipitous sources (omitting the target galaxy) found in this observation is consistent with the expected number of background sources. According to the LogN-LogS function (Hasinger et al. 1993), we would have about 9 sources within a circular area of radius $15'$ and a limiting flux 1.8×10^{-14} erg sec $^{-1}$ cm $^{-2}$ in 0.5-2.0 keV, which corresponds to the faintest among detected sources (Table 2) for a power law spectrum with $\alpha_E = 1$.

Figure 2 provides a close-up view of the NGC 1316 X-ray image which was binned with a pixel size of $2''$ and smoothed with a Gaussian of $\sigma = 4''$, corresponding to FWHM = $11.3''$ for an on-axis point source. This image covers a $3' \times 3'$ field which falls inside the optical galaxy ($12' \times 8.5'$ in $D_{25} \times d_{25}$; see Table 1). Inside the central arcmin, the X-ray emission is elongated along the NE-SW direction, following the optical major axis (PA= 50° ; RC3), while in a larger scale ($\sim 2'$), the X-ray emission is extended along the N-S direction. This extension is more pronounced toward the north (see also Figure 1).

The observed NE-SW elongation inside $r \sim 1'$ is intriguing if real because it may be related to a disk forming in the rotating cooling flow (§4.2) and because the radio jet in projection appears to propagate perpendicular to the direction of this elongation (§4.3). To determine its statistical significance, we first applied a straightforward test by comparing counts and errors in angular sectors at different position angles. We then applied more sophisticated tests: a Monte Carlo simulation and moment analysis. Figure 3 compares the counts at different position angles and gives the significance of differences. Overall the difference between counts extracted in the NE-SW (PA= $30-70^\circ$, $210-250^\circ$) and NW-SE (PA= $120-160^\circ$, $300-340^\circ$) is very significant with a signal to noise ratio of 7.7σ within $r < 40''$.

To estimate whether the flattening of the X-ray isophotes at small radii is due to chance positioning of a few noise ‘blobs’ from an underlying spherical distribution, we have run a Monte Carlo simulation. This involves: (1) choosing a spherical model; (2) creating a set of ‘observations’ in which Poisson noise is added to the model and each X-ray is distributed taking into account the HRI PRF; and (3) then determining the chance probability of occurrence of the observed features. We generated a smooth model image by adopting the X-ray radial profile determined in §2.2 under the assumption of spherical symmetry. Then we normalized the model image and added background counts to match with our HRI observation. We produced a set of 100 ‘observations’ with a pixel size of $2''$ (as in Figure 2) by estimating Poisson deviate for each pixel value and distributing the photon according to the PRF. To estimate how often we obtain an elliptical surface brightness by chance, we examined simulated images after smoothing with the same Gaussian σ as in Figure 2. Out of 100 images, no ellipticity as significant as that of Figure 2 is seen. In our simulations, we also added serendipitous sources at random positions according to the LogN-LogS function (Hasinger et al. 1993) to verify whether a few undetected point sources can mimic our observed features. However the results do not change appreciably. In conclusion, the chance probability to generate the observed, elongated distribution of

the inner X-ray surface brightness out of a circularly symmetrical distribution is less than 1%.

To parameterize the X-ray surface brightness distribution, we have applied a moment analysis (see for details, Buote and Canizares 1994 and Carter and Metcalfe 1980). Ellipticities (ϵ) and position angles of the semi-major axis (θ) are iteratively determined by computing two-dimensional moments of inertia within elliptical apertures. We used an unsmoothed, raw image ($2''$ pixel) with background included. The measured ellipse parameters with a semi-major axis varying from $10''$ to $50''$ are $\epsilon = 0.28 \pm 0.05$ and $\theta = 56^\circ \pm 8^\circ$. We have also applied ellipse fitting (e.g., Jedrzejewski 1987), using the IRAF/STSDAS package to the smoothed image in Figure 2. The derived position angle and ellipticity are consistent with those determined by the moment analysis within their uncertainties.

Figure 4 shows the central region in greater detail with a pixel size of $1''$ and smoothed with a Gaussian of $\sigma = 2''$ which corresponds to an on-axis beam of $6.9''$ FWHM. In this scale the core surface brightness divides into double peaks, separated by $7.3''$. The optical center (RC3) is close (within arcsec) to the X-ray centroid determined with the image in Figure 2 and falls in the middle of the double peaks shown in Figure 4. Also noticeable are larger scale valleys at $PA \simeq 120^\circ$ and $PA \simeq 320^\circ$ which apparently bisect the core if extended to the center.

The double peaks and the SE-NW X-ray valleys are not caused by telescope aspect problems. We used only data obtained in the July run (see Table 1), to avoid a possible mismatch of the galaxy centers in the two observations due to aspect uncertainties, although source positions differ by less than $2''$. The data obtained in the January run also present the same features but with larger statistical noise. To further check potential aspect problems, we applied the same binning and smoothing to point-like sources within the observed field. Sources 4, 7, and 8 which are within $5'$ from the field center [therefore the HRI PRF is similar to the on-axis one (David et al. 1993)] are all circularly shaped while sources 2 and 12, both at $11'$ off-axis distance (the PRF may not be circular), exhibit randomly elongated distribution.

The observed features are very interesting, because the radio jet (Geldzahler and Fomalont 1984) in projection appears to pass through the X-ray valleys (§3). However, the relatively low X-ray counts obtained in this high resolution image may produce an artificial feature by chance positioning of a few noise ‘blobs’. To explore this possibility, we have rerun a Monte Carlo simulation as described above. Out of 100 simulations with

a resolution same as Figure 4 ($1''$ pixel and $\sigma=2''$), 3 images exhibit double peaks and valleys, although not as significant as the observed. This simulation results imply that the existence of the double peaks and the X-ray valleys, although suggestive, is not conclusive and it is required to be confirmed by a deeper observation.

2.2 Radial Profile

Figure 5 shows the radial profile of the X-ray surface brightness measured in concentric rings centered on the NGC 1316 X-ray centroid (Table 2). The raw, background and net counts are indicated by open squares, a solid line and filled squares, respectively. The emission is extended out to $170''$, 22 kpc at the adopted distance of 27.2 Mpc. To this profile, we fitted a King approximation model, $\Sigma_X \sim (1 + (\frac{r}{a})^2)^{-3\beta+0.5}$, convolved with the HRI point response function. [In the case of gaseous emission, β is related to a true isothermal value by $\beta_i = 1.5 \times \beta$ (e.g., Sarazin 1988)]. Best-fit model, fit residuals, and confidence contours are shown in Figure 6. The best fit parameters and 90% confidence range with 2 interesting parameters (in parentheses) are: core radius $a = 4.1''$ (3.1–5.0'') and slope $\beta = 0.51$ (0.49–0.54), yielding $\chi^2 = 14.8$ for 9 degrees of freedom. The estimated slope corresponds to $\Sigma_X \sim r^{-2.06(1.94-2.24)}$ for $r \gg a$. This is close to that of the optical brightness distribution. Using the data in Schweizer (1981), we estimated the slope of the V_4 (5300-6400Å) surface brightness in $r = 30''$ to $300''$ to be 2.02 ± 0.06 . The radial slope measured with the red continuum image (§3) does not differ significantly. We also used the PSPC data to derive the radial profile of the X-ray surface brightness. Using the radial profile within $r=180''$ (to minimize the contribution of extended IC emission; see §2.3 and Feigelson et al. 1995), and a background count rate estimated at $r=1800-2400''$ (with vignetting correction), we find $\Sigma_X \sim r^{-2.25(2.12-2.45)}$, consistent with the HRI profile.

Fits to the radial profiles at the position angles of Figure 3, which take into account the central flattening of the surface brightness give slightly steeper slope [$\beta = 0.56$ (0.52–0.61)] and slightly larger core radius [$a = 6.2''$ (4.1–8.2)] along the direction of flattening, whereas the opposite is true along the perpendicular direction [$\beta = 0.46$ (0.43–0.50) and $a = 1.8''$ (< 3.8)].

A central point source that may be the X-ray counterpart of the radio AGN was not detected with our HRI observations (see the HRI PRF indicated as a dashed line in Figure 5; see also Figure 4). To estimate an upper limit to a central point source, we applied the King model plus the HRI point spread function in fitting the radial profile and determined how strong a central source can be added without having χ^2 too large. We derive an upper

limit (90%) for the central source of about 5% of the total counts, which corresponds to a flux of 1.0×10^{-13} erg sec $^{-1}$ cm $^{-2}$ in 0.1-2.4 keV and a luminosity of 9×10^{39} erg sec $^{-1}$. Here we assumed a power law with an energy index $\alpha_E=0.7$ and line-of-sight N_H . Of course a more luminous AGN would be allowed in the presence of large intrinsic N_H .

The spectral analysis of the extended X-ray emission associated with NGC 1316 (§2.3) suggests that over 60% of the flux is likely to be of gaseous origin. In the assumption that most of the extended emission is due to a hot ISM, we have derived its 3-dimensional density distribution, using a direct deprojection method (Kriss, Cioffi and Canizares 1983), where the emissivity (or density) is inwardly measured by subtracting the contribution of successive spherical layers. We implicitly assume that the hot gas is homogeneous and that the physical status of the gas at a given radius can be represented by one temperature and density. The deprojected density profile is shown in Figure 7a. We have assumed $T = 0.8$ keV (§2.3). The density profile corresponding to $\beta=0.51$, i.e., $n_e \sim r^{-1.53}$ is also shown as a dashed line in the figure.

Using the deprojected density distribution, we estimate the cooling time and gas pressure as a function of radius (Figure 7b). The cooling time is given as $\tau_c = 1.5 \frac{nkT}{n_e n_H \Lambda}$, where n , n_e and n_H are the total particle density, electron density, and Hydrogen density, respectively and Λ is the cooling function. The constant is in the range of 1 to 2.5, depending on its definition (see Sarazin 1988). The cooling time in the center is $\sim 10^8$ years, much smaller than the Hubble time; it reaches 10^{10} years at $\sim 180''$. To estimate the cooling function, we assumed solar metal abundances. With the PSPC spectral data (§2.3), the metal abundances cannot be determined unambiguously (see also e.g., Trinchieri et al. 1994; Fabbiano et al. 1994a). The cooling time in the central region is still much shorter than the Hubble time even with a zero metal abundance model. We also estimate the thermal gas pressure using the measured density and assuming $kT = 0.8$ keV (Figure 8).

We point out that these radial dependences of density, cooling time and pressure are only indicative average values. Because of the complexity of the surface brightness distribution in the inner regions, we would expect a range of these physical parameters at each radius, reflecting the clumpiness of the hot ISM. Also as remarked earlier, we cannot study separately the properties of the different components of the emission suggested by the PSPC data.

2.3 ROSAT PSPC Spectral Properties

In order to determine the X-ray spectral properties, we have used the ROSAT PSPC data obtained from the public archives. The method of data reduction is similar to that of the PSPC observations of NGC 507 (Kim and Fabbiano 1995). Because the X-ray emission is extended at least out to $1000''$ (see Feigelson et al. (1995) for discussions of the extended structure of X-ray emission), we determined the background at $r=1800-2400''$ and applied vignetting correction to each energy channel. Since we are interested in the galaxy emission, we have analyzed the X-ray emission within $180''$ from the center. Feigelson et al. (1995) found Inverse Compton (IC) radiation at the location of the extended radio lobes. The slope of the X-ray radial profile changes abruptly at $r\sim 180''$, indicating that the X-ray emission in the central region has a different origin from that of the extended X-ray emission (Feigelson et al. 1995). To check for possible contribution of IC radiation to the X-ray emission within $r < 180''$, we also estimated the background using portions of the field within the PSPC support structure ($r \sim 1000''$) where the diffuse emission is least. However, the results are not significantly different.

Using XSPEC, we found that the X-ray spectra within $180''$ can be well reproduced either by a one-temperature, low abundance model ($kT \simeq 0.6-0.7$ keV and $\sim 10\%$ solar abundance) or by a two-temperature, solar-abundance model ($kT_1 \simeq 0.1-0.2$ keV and $kT_2 \simeq 0.8-0.9$ keV at 90% confidence). In both cases, the acceptable range of N_H is consistent with the Galactic line-of-sight value (2×10^{20} cm $^{-2}$). The best fit parameters and acceptable ranges with N_H fixed at the line-of-sight value are listed in Table 4. Although we prefer the two-component model rather than the almost zero-abundance model (see §5.1), both models suggest a significant amount of hot gaseous emission, because a significantly higher kT would be expected from a population of LMXB (see the analysis of the M31 bulge data by Fabbiano, Trinchieri and van Speybroeck 1987). We do not see any radial variations in the spectral parameters (temperature and N_H) with the PSPC observations (Table 4).

The absorption-corrected X-ray flux for the best fit parameters is 2×10^{-12} erg sec $^{-1}$ cm $^{-2}$ (see Table 5), corresponding to a X-ray luminosity of 1.8×10^{41} erg sec $^{-1}$ at the adopted distance of 27.2 Mpc. The HRI flux is consistent with the *Einstein* IPC flux (see Table 1). For the two-component model, the X-ray flux of the very soft component is $\sim 40\%$ of the total flux in 0.1-2.4 keV, similar to those seen in other X-ray faint early type galaxies (Fabbiano et al. 1994a, Fabbiano and Schweizer 1995). These results indicate the presence of hot ISM contributing at least 60% of the total X-ray emission even if the soft component is fully of stellar origin.

The analysis of the HRI image (§2.2) shows that a nuclear point source cannot contribute significantly to the emission in the ROSAT band. Therefore the spectral parameters (even in the outermost bin) are representative of an extended emission component. To estimate the upper limits of hard X-ray emission from low-mass binaries to this emission [as seen in the bulges of spirals (Fabbiano 1989) and in ellipticals (Matsushita et al. 1994; Matsumoto et al. 1997)], we added a hard Bremsstrahlung component in the spectral fitting and determined the acceptable range of its normalization. Its temperature was allowed to vary between 3 and 20 keV. The 90% upper limit of the hard component is 15% of the total flux in 0.1-2.4 keV for a one-temperature, low abundance model and 20% for a two-temperature, solar-abundance model. Even if we restrict our analysis to the central 1 arcmin region, the contribution of the hard component is less than 20% for a 1-component model and 30% for a 2-component model. This upper limit corresponds to fluxes of $3 - 4 \times 10^{-13}$ erg sec $^{-1}$ cm $^{-2}$ and luminosities of $3 - 4 \times 10^{40}$ erg sec $^{-1}$ (Table 5). The X-ray to optical luminosity ratio is then $L_X/L_B \leq 2 - 3 \times 10^{29}$ erg sec $^{-1}$ L_\odot^{-1} and is consistent with that of the bulge of M31 where the X-ray emission is dominated by a population of individual bright X-ray sources (e.g., Trinchieri and Fabbiano 1991) and with those of hard components in other early type galaxies observed with ASCA (Matsumoto et al. 1997).

3. COMPARISON WITH OTHER WAVELENGTH DATA

Figures 9, 10 and 11 compare the high resolution HRI contour map of Figure 2 with the distribution of dust (Schweizer 1980), ionized gas, and radio continuum (Geldzahler and Fomalont 1984), respectively. Although the low signal-to-ratio nature of the X-ray data is such that a definitive, quantitative comparison can not be done, there are some qualitative trends that it is worth to mention.

In general, the hot and cold ISM are related in the sense that the X-ray emission is significantly reduced at the locations where the dust patches are more pronounced. In particular, a dust lane is found in the central SE X-ray valley, suggesting the possibility of absorption.

Because the ionized gas may be originated from the cooling hot gas, the distribution of ionized gas provides further clues of the relationship between cold and hot ISM. Narrow-band CCD images were taken on the photometric night of 1994 November 11/12. The CTIO/University of Michigan Curtis Schmidt 0.6/0.9m telescope was used with a Thomson

1024x1024 CCD. Pixel size is $19\mu\text{m}$ square ($1.835''$) however vignetting limits the useable field size to about $30'$. Total exposure times were 8100s each for the redshifted ($v=1801$ km/s) $H\alpha + [\text{NII}]$ (λ 6563 + $\lambda\lambda$ 6548,6583) emission line filter ($\lambda_c = 6606\text{\AA}$, FWHM= 76\AA), and continuum filter ($\lambda_c = 6693\text{\AA}$, FWHM= 81\AA). Bias and dark frames were taken. Flatfields were generated from twilight sky exposures. The spectrophotometric standard HZ 4 was used to calibrate the narrow band images based on AB magnitudes (Oke 1994, private communication). The adopted magnitudes were $\text{AB}_{6606}=15.01$ and $\text{AB}_{6693}=14.81$. The $H\alpha + [\text{NII}]$ image was derived by subtracting a scaled, sky subtracted continuum image from the sky subtracted emission line image. The adopted scaling was calculated from a linear least square fit to residuals of 25 field stars calculated from several scaling factors. The mean pixel value of the $H\alpha + [\text{NII}]$ image at large radii of the optical galaxy was also consistently near zero. The distribution of ionized gas is shown in Figure 10, superposed on the X-ray image (same as Figure 2). The overall distribution of the ionized gas is similar to that of the dust, ie., aligned toward north-south, slightly turned to NW and SE (clockwise), as observed in other early type galaxies with cold ISM (Kim 1989). The peak of the northern blob ($40^s.5$, $11'.8$) falls in between the dust patches, likely due to dust absorption. The eastern part of the southern blob generally follows the distribution of the dust patch. Comparing the distributions of hot and warm ISM, we also find an overall similarity (e.g., N-S extension), but there is not always a one-to-one correspondence.

Figure 11a shows the radio jets superposed on the X-ray image (same as Figure 2). This radio image was reproduced from the Figure 2b in Geldzahler and Fomalont (1984), which was obtained with the VLA and has $4''$ resolution at 1.5 GHz. The direction of the radio jet is in projection perpendicular to the direction of NE-SW elongation of the central X-ray distribution. If confirmed, the X-ray valleys (seen in Figure 4) may imply even more striking relations in that both sides of the radio jets in projection coincide with the X-ray valleys at $\text{PA}\simeq 120^\circ$ and $\text{PA}\simeq 320^\circ$ (Figure 11b), suggesting that the radio jets are interacting with the surrounding hot gaseous medium as seen in Cygnus A (Carilli, Perley and Harris 1994).

These connections need to be checked with future high resolution observations. The AXAF CCD detector will provide $1''$ resolution data with spectral resolution as well, which will be ideally suited for this type of investigation.

4. DISCUSSION

4.1 The Nature of X-ray Emission of NGC 1316

The X-ray emission of E and S0 galaxies can be due to different sources (see Fabbiano 1989): a hot gaseous halo dominating the emission in the X-ray bright early type galaxies; integrated stellar X-ray binary emission, seen in the bulges of spirals (see Fabbiano 1989) and confirmed in ellipticals with ASCA (Matsushita et al. 1994; Matsumoto et al. 1997); a nuclear source, seen in bright radio galaxies (Fabbiano et al. 1984; Worrall and Birkinshaw 1994); and a very soft component, seen in X-ray-faint early type galaxies (Kim et al. 1992b; Fabbiano et al. 1994a; Kim et al. 1996) of debatable nature (e.g., Pellegrini and Fabbiano 1994). NGC 1316 is both an X-ray faint D (maybe cD) galaxy and a radio galaxy, therefore its X-ray emission is likely to be complex.

With the HRI imaging data and the PSPC spectral data, we can limit the contribution from the nuclear component and stellar binary component respectively as being relatively unimportant to the detected X-ray emission (Table 5). The upper limit to the nuclear X-ray emission obtained with the HRI image (§2.2) is $L_X \leq 9 \times 10^{39}$ erg sec⁻¹, which is about 5% of the total luminosity. Of course a more luminous nuclear source could be present and not visible if the nuclear N_H is much higher than the line of sight one. With the PSPC spectra, we can pose an upper limit to the hard stellar component of 20-30% of the total flux in 0.1-2.4 keV ($L_X \leq 3 - 4 \times 10^{40}$ erg sec⁻¹; §2.3). This is consistent with the expected hard X-ray emission from a 'bulge' population of X-ray sources (e.g., scaling from the M31 bulge; Trinchieri and Fabbiano 1991). Individual typical X-ray binary sources would not be detectable at the luminosity threshold of our observation (a few $\times 10^{39}$ erg sec⁻¹).

The PSPC spectrum of NGC 1316 (§2.3) suggests that most of the X-ray emission within 3' is due to a hot ISM in this galaxy. Although with the PSPC data we cannot unequivocally define the emission model, the spectral fits require the presence of a $\sim 0.7-0.9$ keV thermal emission (Table 4). The X-ray spectrum of NGC 1316 resembles that of other X-ray faint early type galaxies. X-ray spectra of those galaxies observed both with the IPC (Kim et al. 1992a) and the PSPC (e.g., Fabbiano et al. 1994a) present an excess of counts in the lowest energy channels, when compared to those of X-ray bright E and S0. This type of spectrum can either be fitted with a metal-free single-temperature optically-thin model, or with two (or more) component models (see Fabbiano et al. 1994a; Pellegrini and Fabbiano 1994; Fabbiano and Schweizer 1995). Recent ASCA measurements of the spectrum of the X-ray faint galaxy NGC 4382 (Kim et al. 1996) reject the single-component metal-free model in that galaxy. The two component model, in the case of NGC 1316, would consist of a very soft component of kT $\sim 0.1-0.2$ keV (which could be of stellar origin, e.g., Pellegrini and Fabbiano 1994), and a harder (kT $\sim 0.7-1.0$ keV), almost solar

metallicity ISM. It is interesting that the abundance of the ISM determined from this two-component model is near to the optical metallicity of this galaxy (e.g., Gorgas, Efsthathiou and Salamanca 1990). However, based on more general ASCA results on galaxies (e.g., Loewenstein et al. 1994; Arimoto et al. 1996), the latter may just be a coincidence.

Although a hot ISM is present, the total amount of hot gas is $\sim 10^9 M_\odot$, only a fraction of that present in X-ray bright early type galaxies with a comparable optical luminosity (for example, $M_{gas} \sim 2 \times 10^{10} M_\odot$ in NGC 4636; Trinchieri et al. 1994). NGC 1316 clearly has not been accumulating all the gas ejected from the evolved stars during a Hubble time, which would be $\sim 3 \times 10^{10} M_\odot$. This is not surprising since this galaxy may have undergone recent merging events (see Schweizer 1980). Recent mergers (Hibbard et al. 1994) and dynamically young ellipticals (Fabbiano and Schweizer 1995) also tend to be relatively empty of hot ISM. It may be a coincidence, but the mass of the hot ISM is comparable with what would be expected from stellar accumulation in ~ 1 Gyr, which may be the age of merger (Schweizer 1980). In a recent paper discussing the optical and X-ray emission at larger radii, Mackie and Fabbiano (1997) find $\sim 3 \times 10^8 M_\odot$ of hot ISM spatially coincident with the tidal tails in the outskirts of NGC 1316.

4.2 Multi-phase ISM

The comparison between X-ray and optical data reveals that the distribution of the X-ray emission is related with that of dust patches (§3.1.). The X-ray emission is weak where dust is seen and X-ray blobs are often surrounded by dust patches. The X-ray valleys running toward NW and SE from the center (Figure 4), if confirmed, may be real low density regions in the hot ISM, because they are not coincident with dust patches, except in the central SE region. The ionized gas is overall cospatial with the dust patches. However, the northern blob of the ionized gas falls in between dust patches, while the southern blob coexists with dust, indicating some of the line emission is absorbed by the dust.

The origin of the ionized gas (i.e., ionization mechanism) is unclear in early type galaxies. The emission lines often indicate LINER-type nuclear activity rather than HII regions, judged by for example the relative line strengths $H\alpha$ to [NII] flux ratio (e.g., Kim 1989). It has also been suggested that the gas is photo-ionized by post AGB stars (Trinchieri and di Serego Alighieri 1991). In the case of galaxies containing significant amounts of hot ISM, the ionized gas may also be the result of cooling flows (e.g., Sarazin 1988), but this is unlikely in NGC 1316.

In NGC 1316, the kinematics of the ionized gas revealed that the gas is rapidly (up to 350 km sec^{-1}) rotating along the minor axis (PA=127-142°; Schweizer 1980), while the stellar system rotates along the major axis (PA=50°; Bosma, Smith and Wellington 1985). The same is true for molecular gas (Sage and Galletta 1993). This suggests an external origin for the cold and ionized ISM, perhaps connected with the merging episode (Schweizer 1980; Mackie and Fabbiano 1997) and argues against the idea that the ionized/cold gas is originated from cooling hot gas. In the latter case both hot and cold/warm gas would be expected to have the same kinematics as the stars, since the hot ISM is likely to originate from stellar evolution. Different origins of warm gas (likely cold gas and dust as well) and hot gas may be further supported by our HRI observations in that the central X-ray flattening, possibly a disk would rotate along the major axis and that the morphological relationships between the ionized gas and the X-ray emission are lacking. Therefore, it is likely that the cold and warm ISM might be acquired externally by mergers and infalls occurred $\sim 10^9$ years ago, while the hot gas has been accumulated since the latest merger.

If the infalling, cooling hot ISM carries angular momentum it may form an accretion disk, which could be extending out to a 10 kpc radius (see Kley and Mathews 1995; Brighenti and Mathews 1996). The NE-SW flattened isophotes of NGC 1316 (Figure 2) may represent such a disk. However, because the isophotes are measured at radii less than the optical effective radius, the stellar potential needs not be round at these radii. Therefore, the observed elongation may be consistent with hydrostatic gas in the stellar potential (or with a modest amount of dark matter).

4.3 Is the radio jet thermally confined?

Interestingly, the observed elongation in the hot gas structure is approximately perpendicular to the radio jet of NGC 1316. The possibility of thermal confinement is supported by the radial behaviour of the jet/ISM energetics. We estimated the radio jet pressure corresponding to the minimum energy using the radio map by Geldzahler and Fomalont (1984) (see Feigelson et al. 1995 for the validity of the minimum energy argument). We applied the prescription for a Gaussian jet given in Killeen, Bicknell and Ekers (1986a; see also Pacholczyk 1970). We also used the cylindrical jet approximation (see Perley, Willis and Scott 1979), but the results do not change significantly. We assumed that: the jet and the magnetic field are perpendicular to the line of sight; the energy of relativistic electrons is equal to that of protons and ions; the radio spectrum is a power law from 10 MHz to 10 GHz with a slope $\alpha=0.7$; and the volume filling factor is unity. The estimated jet pressure is compared with the thermal pressure in Figure 8. At 6 - 24'' from the cen-

ter, the jet pressure for both NW and SE jets is an order of magnitude lower than the thermal pressure. Radio and thermal pressure are supposed to be in balance in the case of thermal confinement. However, as discussed by Killeen et al. (1988) the radio minimum pressure could be easily underestimated (see also Pacholczyk 1970) while the similarity of the radial behaviour of radio and X-ray pressures argues for thermal confinement. This apparent contradiction between the thermal gas and minimum radio pressures has also been reported in similar cases where radio jets are expanding through the hot gaseous environment (e.g., Bohringer et al. 1993; Carilli, Perley and Harris 1994).

The possibility (suggested by Figure 8) that the jet is thermally confined inside a relatively small region reinforces the suggested lack of causal connection between the jet and the extended lobes (Ekers et al. 1983). It is possible that active events took place some time ago, probably induced by a merger ($\sim 10^9$ years ago; Schweizer 1980) and now the nucleus is relatively weak and the radio lobes are slowly cooling (see also Ekers et al. 1983). This idea is also supported by the relative power ($\sim 1/2500$) of the jets to the extended radio lobes, which is a few hundred times lower than that of a typical early type galaxy (Slee et al. 1994); the lack of strong optical emission lines (see Schweizer 1980); the absence of a connection between the jet and the lobe (Geldzahler and Fomalont 1984); and the morphology of the lobes (Fomalont et al. 1989).

The double peaks and X-ray valleys seen in Figure 4, if confirmed, will provide more direct evidence for interaction between the hot gas and the radio jet. Both sides of the radio jets in projection appear to pass through the X-ray valleys which may play a role as nozzles in collimating the jets.

4.4 The Nucleus

Fabbiano et al. (1984) found a relationship between radio core power and X-ray luminosity in a sample of 3CR galaxies, indicating that both radio and X-ray emission are of non-thermal nuclear origin. This relationship holds down to radio faint galaxies (Fabbiano et al. 1989). Recently, with ROSAT observations, Worrall and Birkinshaw (1994) spatially decomposed central X-ray point sources from the diffuse, extended emission in several radio galaxies and confirmed the linear relationship between core radio and central X-ray emission in low-power radio galaxies. Although the X-ray core of NGC 1316 is not detected, the ratio between the X-ray upper limit (corresponding to $l_{1keV} \leq 6.3 \times 10^{21}$ erg s $^{-1}$ Hz $^{-1}$) and the radio core emission ($l_{5GHz} = 2 \times 10^{28}$ erg s $^{-1}$ Hz $^{-1}$, from Geldzahler and Fomalont 1984) is consistent with the linear relationship between these quantities discussed above.

A comparison of the spectral energy distribution (SED) of the NGC 1316 nucleus with those of other LINER galaxies can be found in Fabbiano and Juda (1997). It is worth noting the possible similarity between the nuclear sources of NGC 3998 and NGC 1316 (both early type galaxies). They both present a bright UV point-like source discovered with HST, and their SED differ from those of bright AGN (see also Fabbiano et al. 1994b). A better coverage of the nuclear emission of these faint AGN will be necessary to understand the emission mechanism.

5. CONCLUSION

We have presented the analysis of the high spatial resolution image and of the X-ray spectrum of NGC 1316 (Fornax A) obtained with the ROSAT HRI and PSPC. The results lead to the following conclusions:

(1) The X-ray emission of NGC 1316 is extended. No point sources are detected within the galaxy at a luminosity threshold of a few $\times 10^{39}$ erg sec $^{-1}$. The radial profile of the X-ray surface brightness falls as r^{-2} , which is close to the optical light distribution. No gradient of the X-ray emission temperature is seen. Within the central 40'', the X-ray isophotes are flattened along the optical major axis. In a larger scale (1-2'), the X-ray emission is extended toward N-S, in agreement with the PSPC report of Inverse Compton emission (Feigelson et al. 1995).

(2) The X-ray spectrum of NGC 1316 ($r < 180''$) can be reproduced either by a single-temperature low-abundance model ($kT = 0.7$ keV and 10% solar) or by a two-temperature, solar-abundance model ($kT_1 = 0.1-0.2$ keV and $kT_2 = 0.8-0.9$ keV). These results indicate the presence of hot gaseous component contributing to $>60\%$ of the total X-ray emission. We set an upper limit of $\sim 20\%$ of the total emission due to a hard component from LMXB in NGC 1316, consistent with an extrapolation based on the bulge of M31 as well as those of early type galaxies observed with ASCA. The total X-ray emission is 2×10^{41} erg sec $^{-1}$ in the 0.1-2.4 keV band and $M_{gas} \sim 10^9 M_{\odot}$. The relatively small amount of hot ISM present in this X-ray faint galaxy [by comparison with that of X-ray bright E and S0 such as NGC 4636 and NGC 4472 (e.g., Fabbiano et al. 1992)] is consistent with observations of other systems that may have undergone relatively recent merging (Fabbiano and Schweizer 1995).

(3) The X-ray emission is significantly reduced at the locations where the dust patches

are more pronounced, indicating that some of the X-ray emission may be absorbed by the internal cold ISM in NGC 1316. The ionized gas is generally distributed along with the dust patches. Some features of the ionized gas appear to be related with a hot ISM but there is no one-to-one correspondence. Both morphological relations and kinematics suggest that the hot and cold/warm ISM may not have the same origin. The cold/warm ISM might be acquired externally by mergers/infalls, while the hot ISM has been accumulated since the latest merger.

(4) In projection, the direction of the radio jets is perpendicular to the central NW-SE elongation of the X-ray emission. The thermal pressure is higher than the jet equipartition pressure by an order of magnitude. However, the radial behaviour of thermal and radio pressures are similar, suggesting the possibility of thermal confinement.

(5) Although a nuclear source is not detected in X-rays, the upper limit ($L_X \leq 9 \times 10^{39}$ erg sec⁻¹) is consistent with the expectations, based on the extrapolation from low-power radio galaxies (Worrall and Birkinshaw 1994).

ACKNOWLEDGMENTS

This work was supported by NASA grants NAG 5-2152 (ROSAT), NAGW 2681 (LTSA), NASA contract NAS8-39073 (AXAF Science Center) and by Non Directed Research Fund, Korea Research Foundation. This research has made use of SIMBAD which is operated by the Centre de Donnees astronomiques de Strasbourg (CDS), France. We thank the referee and Greg Bothun for their comments on the original draft.

REFERENCES

- Arimoto, N., Matsuchita, K., Ishimaru, Y., Ohashi, T., & Renzini, A. 1996 preprint
- Arp, H. 1966, ApJS, 14, 1
- Baum, S. A., Heckman, T. M. & van Breugel, W. 1992, ApJ, 389, 208
- Begelman, M. C., Blandford, R. D., & Rees, M. J. 1984, Rev. Mod. Phys. 56, 255
- Bohringer, H., Voges, W., Fabian, A. C., Edge, A. C., & Neumann, D. M. 1993, MNRAS, 264, L25
- Bosma, A., Smith, R. M. & Wellington, K.J. 1985, MNRAS, 212, 301
- Brightenti, & Mathews, W. 1996, preprint
- Buote, D. A., & Canizares, C. R. 1994, ApJ, 427, 86.
- Carilli, C. L., Perley, R. A., & Harris, D. E. 1994, MNRAS, 270, 173
- Carter, D., Jorden, P.R., Thorne, D.J., Wall, J.V. & Straede, J.C. 1983 MNRAS, 205, 377
- Carter, D., and Metcalfe, N. 1980, MNRAS, 191, 325
- David, L. P., Harnden, F. R., Kearns, K. E., & Zombeck, M. V. 1993, The ROSAT High Resolution Imager (US ROSAT Science Data Center/SAO)
- de Vaucouleurs, G., de Vaucouleurs, H., Corwin, H. G., Buta, R. J., Paturel, G., & Fouque, P. 1991 *Third Reference Catalogue of Bright Galaxies, (RC3)*, (New York: Springer-Verlag)
- Ekers, R. D., Gross, W. M., Wellington, K. J., Bosma, A., Smith, R. M., & Schweizer, F. 1983, AA, 127, 361
- Fabbiano, G. 1989, ARAA, 27, 87
- Fabbiano, G., Miller, L., Trinchieri, G., Longair, M., & Elvis, M. 1984, ApJ, 277, 115
- Fabbiano, G., Gioia, I. M., & Trinchieri, G. 1988, ApJ, 324, 749
- Fabbiano, G., Gioia, I. M., & Trinchieri, G. 1989, ApJ, 347, 127
- Fabbiano, G., Kim, D.-W., & Trinchieri, G. 1992, ApJS, 80, 531
- Fabbiano, G., Kim, D.-W., & Trinchieri, G. 1994a, ApJ, 429, 94
- Fabbiano, G., Fassnacht, C., & Trinchieri, G., 1994b, ApJ, 434, 67
- Fabbiano, G., & Schweizer, F. 1995, ApJ, 447, 572
- Fabbiano, G., & Juda, G. 1997, in preparation.
- Fabbiano, G., Trinchieri, G., and van Speybroeck, L. 1987, ApJ, 316, 127
- Faber, S. M., and Gallagher, J. S. 1979, ARAA, 17, 135
- Feigelson, E.D., Laurent-Muehleisen, S.A., Kollgaard, R.I., & Fomalont, E. B. 1995, ApJ, 449, L149
- Fomalont, E. B., Ebnerter, K. A., van Breugel, J. M., & Ekers, R. D. 1989, ApJ, 346, L17
- Geldzahler, B. J., & Fomalont, E. B. 1984, AJ, 89, 1650

- Gorgas J., Efstathiou G. & Aragon Salamanca, A. 1990, MNRAS, 245, 217
- Hasinger, G., Burg, R., Giacconi, R., Hartner, G., Schmidt, M., Trumper, J., & Zamorani, G. 1993, AA, 275, 1
- Hibbard, J. E., Guhathakurta, P., van Gorkom, J. H., Schweizer, F. 1994, AJ, 107, 67
- Jedrzejewski, R. I. 1987, MNRAS 226, 747
- Kaneda, H., Tashiro, M., Ikebe, Y., Ishiki, Y., Kubo, H., Makishima, K., Ohashi, T., Saito, Y., Tabara, H., and Takahashi, T. 1995, ApJ, 453, L13
- Killeen, N. E. B., Bicknell, G. V., & Ekers, R. D. 1986a, ApJ, 302, 306
- Killeen, N. E. B., Bicknell, G. V., & Carter, D. 1986b, ApJ, 309, 45
- Killeen, N. E. B., Bicknell, G. V., & Ekers, R. D. 1988, ApJ, 325, 180
- Kim, D.-W. 1989, ApJ, 346, 653
- Kim, D.-W., Fabbiano, G., & Trinchieri, G. 1992a, ApJS. 80, 645
- Kim, D.-W., Fabbiano, G., & Trinchieri, G. 1992b, ApJ. 393, 134
- Kim, D.-W., & Fabbiano, G., 1995, ApJ, 441, 182
- Kim, D.-W., Fabbiano, G., Matsumoto, H, Koyama, K., & Trinchieri, G. 1996, ApJ, 468, 175.
- Kley, W. & Mathews, W. 1995, ApJ, 438, 100
- Knapp, G. R., Turner, E. L., & Cunniffe, P. E. 1985, AJ, 90, 454
- Knapp, G. R., Guhathakurta, P., Kim, D.-W., & Jura, M. 1989, ApJS, 70, 329
- Kriss, G. A., Cioffi, D. F., & Canizares, C. R. 1983, ApJ, 272, 439
- Loewenstein, M., Mushotzky, R. F., Tamura, T., Ikebe, Y., Makishima, K., Matsushita, K., Awaki, H., & Serlemitsos, P. J. 1994, ApJ, 436, L75.
- Mackie, G., & Fabbiano, G. 1997, AJ submitted
- Malin, D. F., & Carter, D. 1983, ApJ, 274, 534
- Matsushita, K., Makishima, K., Awaki, H., Canizares, C. R., Fabian, A. C., Fukazawa, Y., Loewenstein, M., Matsumoto, H. Mihara, T., Mushotzky, R. F., Ohashi, T., Ricker, G. R., Serlemitsos, P. J., Tsuru, T., Tsusaka, Y., & Yamazaki, T 1994, ApJ, 436, L41
- Matsumoto, H., Koyama, K., Awaki, H., Tsuru, T., Loewenstein, M., and Matsushita, K. 1997, ApJ, 482, 133.
- Pacholczyk, A. G. 1970, *Radio Astrophysics* (San Francisco: Freeman)
- Pellegrini, S. & Fabbiano, G. 1994, ApJ, 429, 105
- Perley, R. A., Willis, A. G., & Scott, J. S. 1979, Nature, 281, 437
- Phillips, M. M., Jenkins, C. R., Dopita, M. A., Sadler, E. M. & Binette, L. 1986, AJ, 91, 1062
- Sage, L.J. & Galletta, G., 1993, ApJ, 419, 544
- Sarazin, C. L. 1988 *X-ray emissions from clusters of galaxies* (Cambridge: Cambridge

University press)

Schweizer, F., 1980, ApJ, 237, 303

Schweizer, F., 1981, ApJ, 246, 722

Slee O. B., Sadler E. M., Reynolds, J. E. & Ekers R.D. 1994, MNRAS, 269, 928

Truemper, J. 1983, Adv. Space Res. 2, 241

Trinchieri, G. & Fabbiano, G. 1991, ApJ, 382, 82

Trinchieri, G. & di Serego Alighieri, S. 1991, AJ, 101, 1647

Trinchieri, G., Kim, D.-W., Fabbiano, G. & Canizares, C. R. 1994, ApJ, 428, 555

Veron-Cetty, M. P. & Veron, P. 1986 , AAS, 66, 335

Wade, C. M. 1961, Pub. NRAO, 1, 99

Wiklind, T. & Henkel, C. 1989, AA, 225, 1

Worrall, D. M., & Birkinshaw, M. 1994, ApJ, 427, 134

Table 1
Basic parameters

	NGC 1316	NGC 1317
RA (J2000) ^a	3 22 41.6	3 22 44.7
DEC (J2000) ^a	-37 12 28	-37 6 10
B _T ^o (mag) ^a	9.40	11.81
D (Mpc) ^b	27.2	27.2
D ₂₅ (arcsec) ^a	721	165
N _H (cm ⁻²) ^c	2.0 x 10 ²⁰	2.0 x 10 ²⁰
HRI Observed Date ^d	Jan. 14, 1994	Jan. 14, 1994
HRI Exp time (sec) ^d	11038	11038
HRI Observed Date ^e	Jul. 7-10, 1994	Jul. 7-10, 1994
HRI Exp time (sec) ^e	29403	29403
PSPC Observed Date	Jan. 13-20, 1992	Jan. 13-20, 1992
PSPC Exp time (sec)	25500	25500
Log Fx (IPC) erg sec ⁻¹ cm ^{-2f}	2.0 x 10 ⁻¹²	<2.7 x 10 ⁻¹³

a. Right Ascension (RA), declination (DEC), total face-on B magnitude (B_T^o), and major isophotal diameter measured at B = 25 magnitude arcsec⁻²(D₂₅) taken from de Vaucouleurs et al. 1991 (RC3)

b. Distance from Fabbiano et al. 1992.

c. Galactic line of sight HI column density from Starks et al. 1992.

d. Sequence number 600255n00

e. Sequence number 600255a01

f. IPC flux from Fabbiano et al. 1992. Fluxes were estimated in a energy range of 0.2–4.0 keV for a Raymond-Smith model with solar abundance, kT=1keV and line of sight N_H. The count extraction radii are r=450'' for NGC 1316.

Table 2
X-ray sources

source number	X Y pixel	radius ^c arcsec	offaxis arcmin	vignetting correction	net cnts	error	Fx ^e 10 ⁻¹³
1	5599.86 3823.70	30	12.9	1.076	67.44	15.77	0.53
2	5075.38 4998.42	25	10.9	1.055	89.45 ^d	14.96	0.69
3	4468.47 4499.67	30	4.4	1.012	48.61	15.52	0.36
4	4104.82 3607.70	25	4.7	1.013	86.11	15.30	0.64
5 ^a	4076.98 4108.50	170	—	—	2047.79	85.77	14.99
6 ^b	4009.78 4862.26	20	6.2	1.020	120.29	15.05	0.90
7	3842.10 4436.98	25	3.4	1.008	35.52	13.19	0.26
8	3702.10 3687.70	30	5.1	1.015	68.92	16.08	0.51
9	3296.79 3583.91	15	8.1	1.033	31.89	9.79	0.24
10	3041.20 3157.04	25	12.0	1.065	53.90	13.76	0.42
11	2959.06 4396.66	20	9.7	1.045	44.42	11.83	0.34
12	2823.38 3703.22	20	11.2	1.057	201.14 ^d	17.81	1.56

a. NGC 1316

b. NGC 1317

c. Background counts were extrated in annuli (r=200''- 400'' for NGC 1316; r=60''-200'' for all other sources).

d. variable (see Table 3).

e. Fluxes were estimated in a energy range of 0.1–2.4 keV for a Raymond-Smith model with solar abundance, $kT = 1$ keV and line of sight N_H . Vignetting correction was applied.

Table 3
Variable Sources

source	Jan. 94		Jul. 94		difference
number	rate	err	rate	err	σ
2	-0.47	0.56	3.22	0.46	5.09
12	7.81	1.04	3.92	0.46	3.41

Rates and errors are in unit of counts in 1,000 seconds.

TABLE4

TABLE5

Figure Captions

Figure 1. The entire field of view of this HRI observation (NGC 1316 and NGC 1317). The X-ray contours are overlaid on the optical image obtained from the Digital Sky Survey. X-ray image is binned with a pixel size of 8 arcsec, background-subtracted and smoothed with a Gaussian of $\sigma = 16$ arcsec. The octagonal shape indicates the boundary of the HRI detector. The source numbers are ordered by an increasing RA (see Table 2). RA and Dec are in J2000.

Figure 2. A close-up view of the X-ray image (with a pixel size of $2''$ and a Gaussian σ of $4''$). The contours indicate isophotes at 5% to 95% of the peak with 8 steps. RA and Dec are in J2000.

Figure 3. (a) Radial distribution of X-ray counts extracted in different angular sectors. The filled circles are for the NE-SW sector (PA=30-70°, 210-250°) and the open circles are for NW-SE (PA=120-160°, 300-340°). (b) The significance of count differences between two angular sectors.

Figure 4. same as Figure 2 but with a pixel size of $1''$ and a Gaussian σ of $2''$. The data obtained only in the July run are used. The contours indicate isophotes at 6% to 85% of the peak with 8 steps.

Figure 5. Radial distribution of X-ray counts determined with the raw, unsmoothed image. Raw, background (determined at $r=200-400''$), and net counts are indicated by open squares, a solid line and filled squares with error bars.

Figure 6. Radial profile of X-ray surface brightness and best fit model prediction.

Figure 7. (a) Deprojected density and (b) cooling time as a function of radius. The density profile corresponding to $\beta=0.51$ ($n_e \sim r^{-1.53}$) is shown as a dashed line.

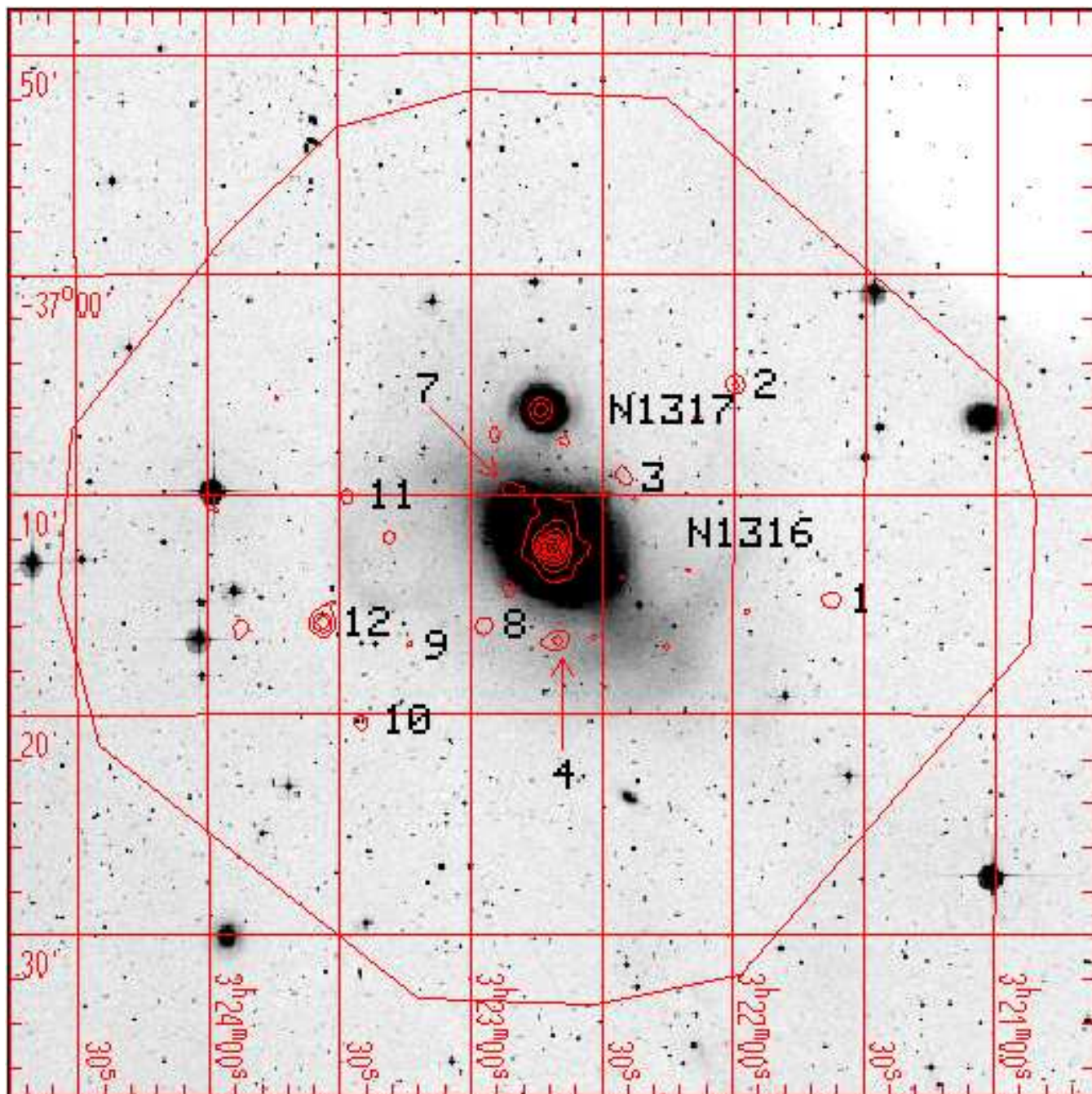
Figure 8. Thermal gas pressure as a function of radius. The minimum radio pressure along the jets is also plotted with filled circles (the NW jet) and open circles (the SE jet).

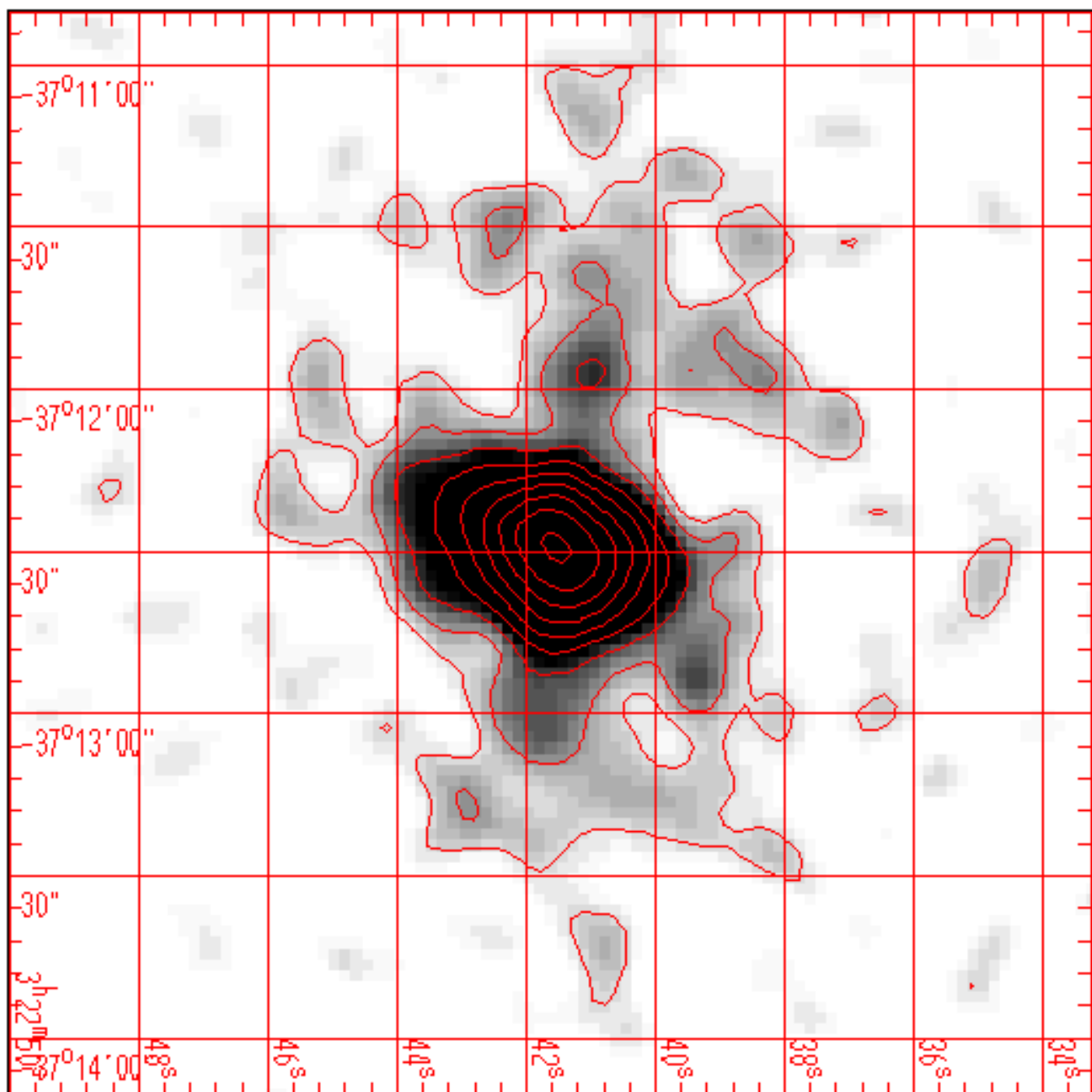
Figure 9. Distribution of dust patches (from Schweizer 1980) overlaid onto the X-ray image (same as Figure 2).

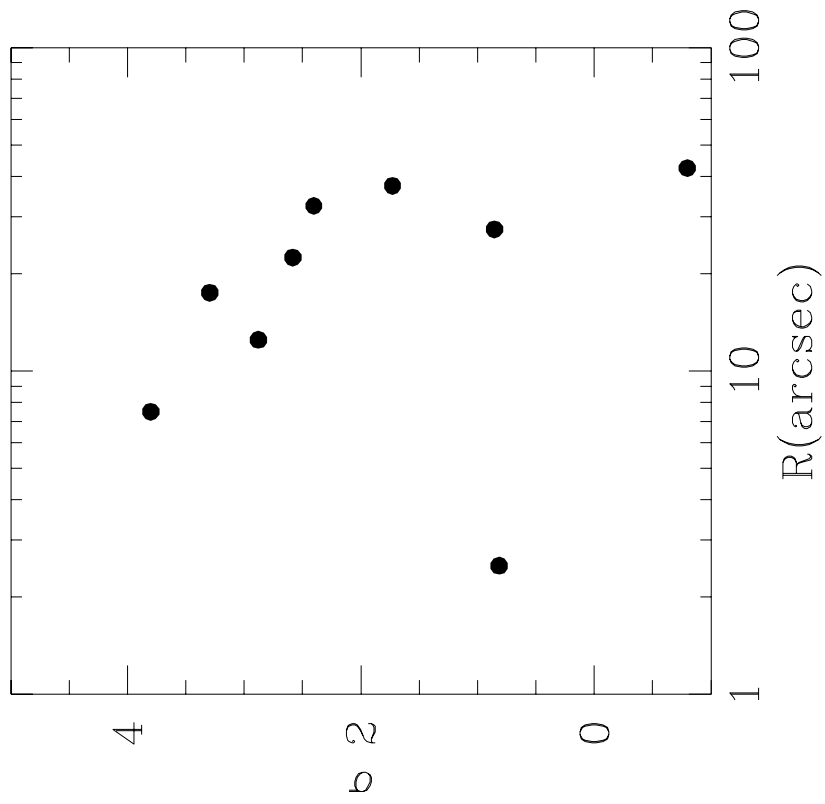
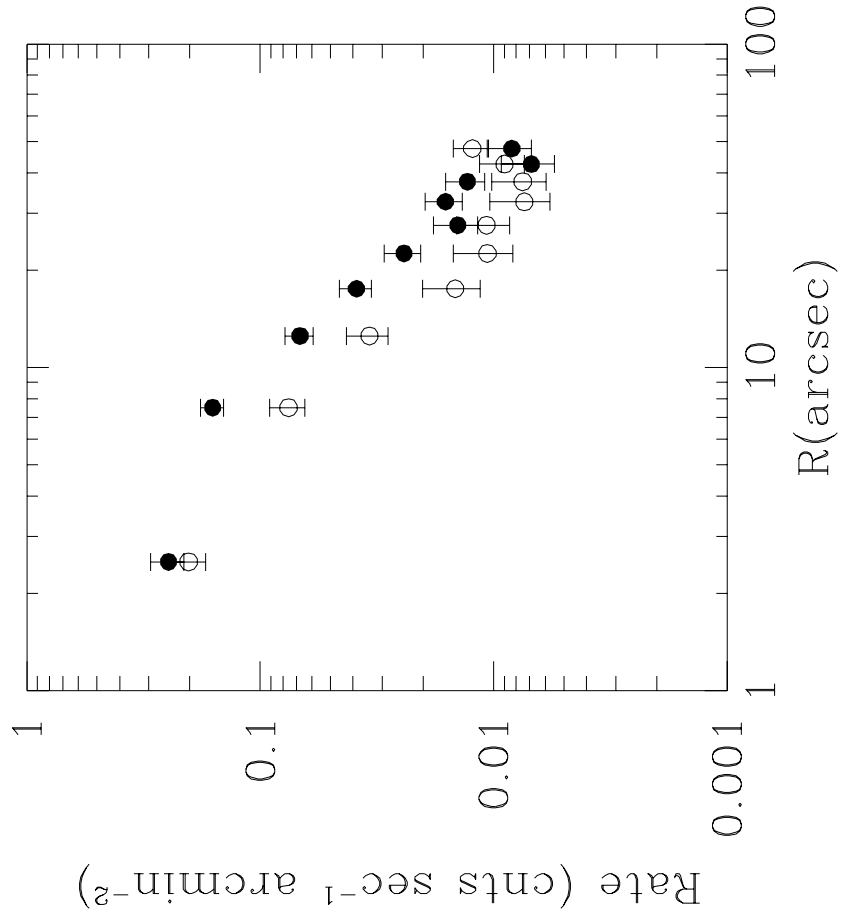
Figure 10. Distribution of ionized gas overlaid onto the X-ray image. The continuum-subtracted $H\alpha + [\text{NII}]$ image was smoothed with a 2 pixel (full width) gaussian filter

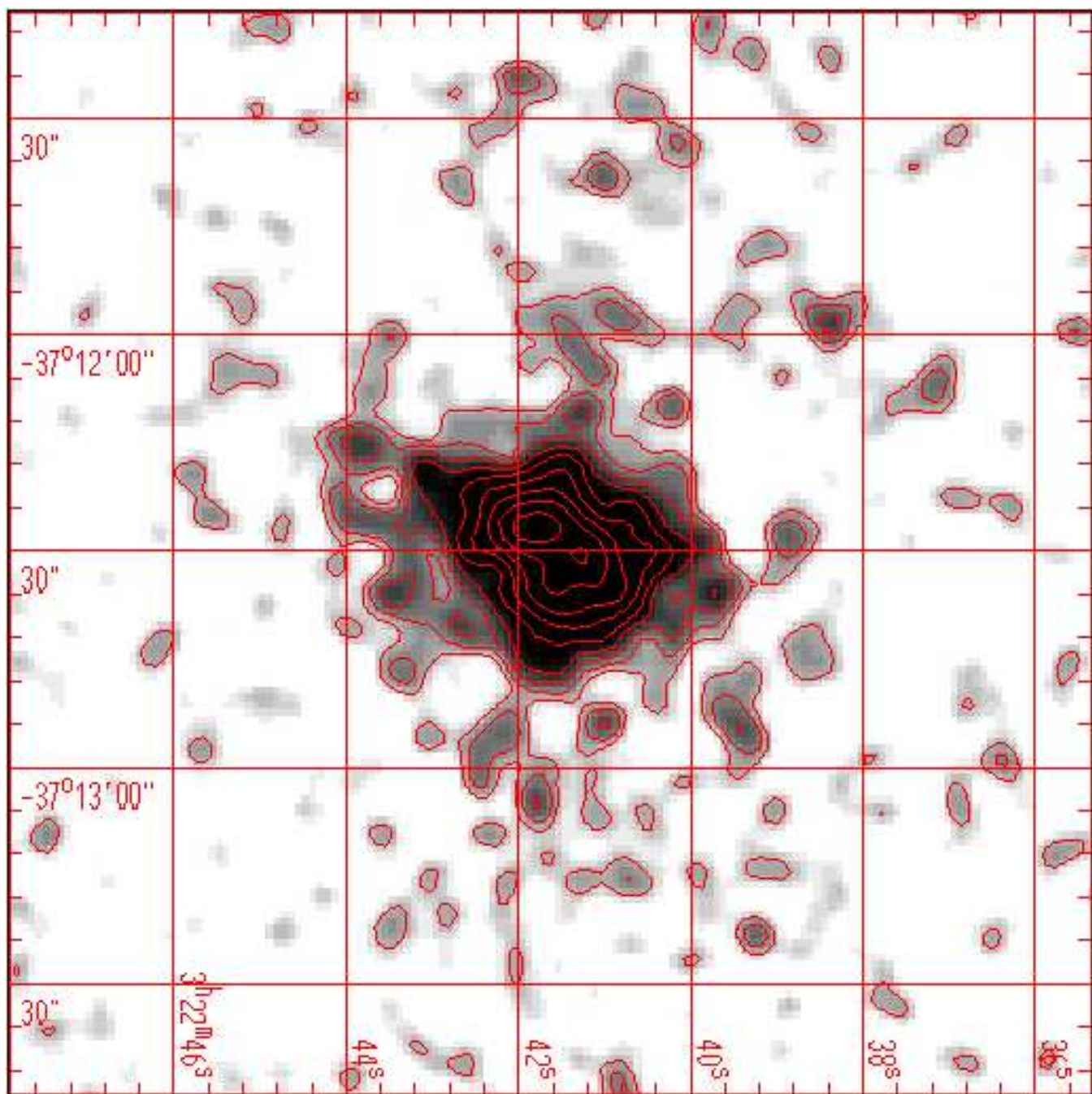
and the X-ray image is the same as Figure 2.

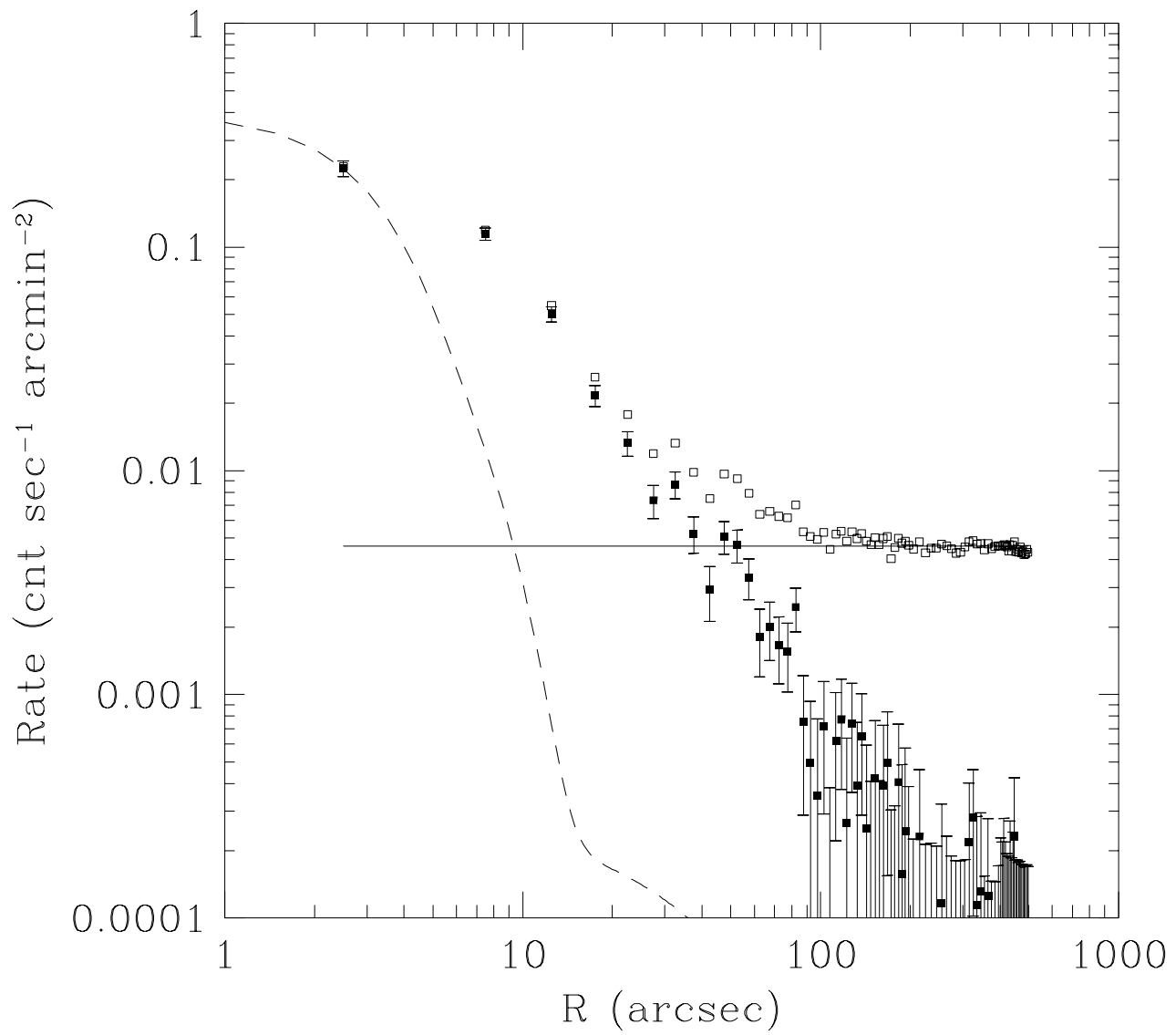
Figure 11. Radio jet overlaid onto the X-ray image. The radio map was taken from Geldzahler and Fomalont (1984). The X-ray image is the same as (a) Figure 2 and (b) Figure 4.

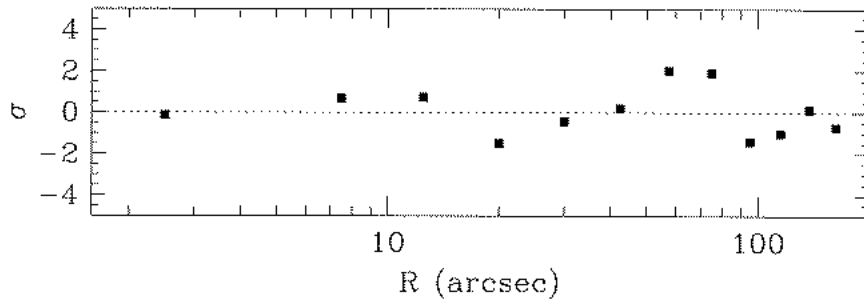
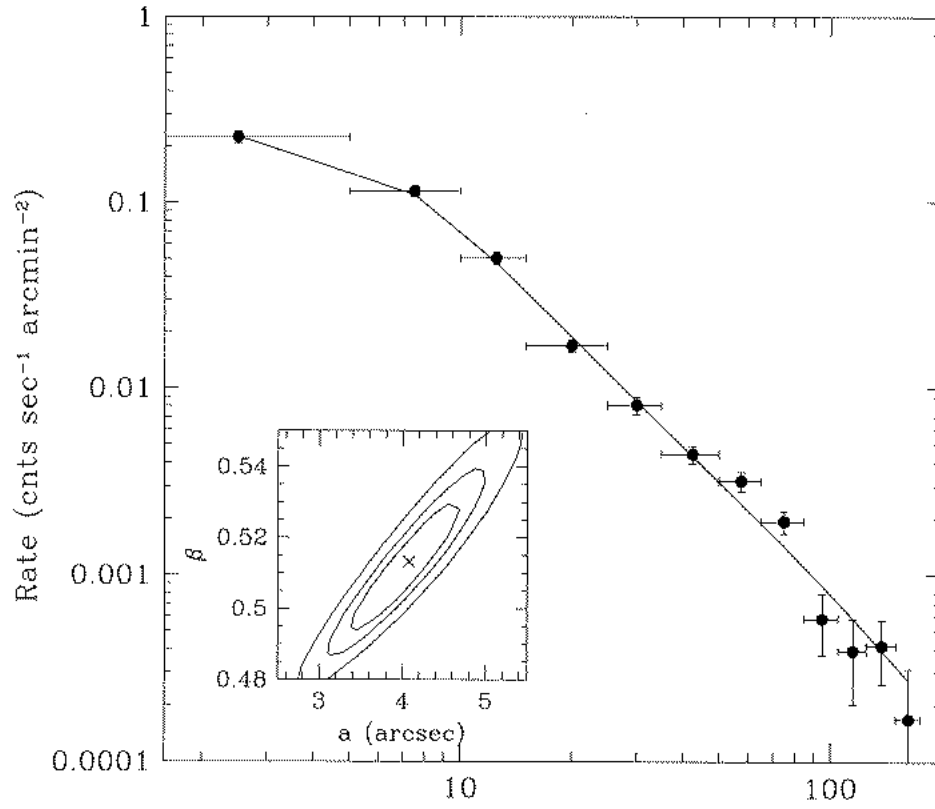


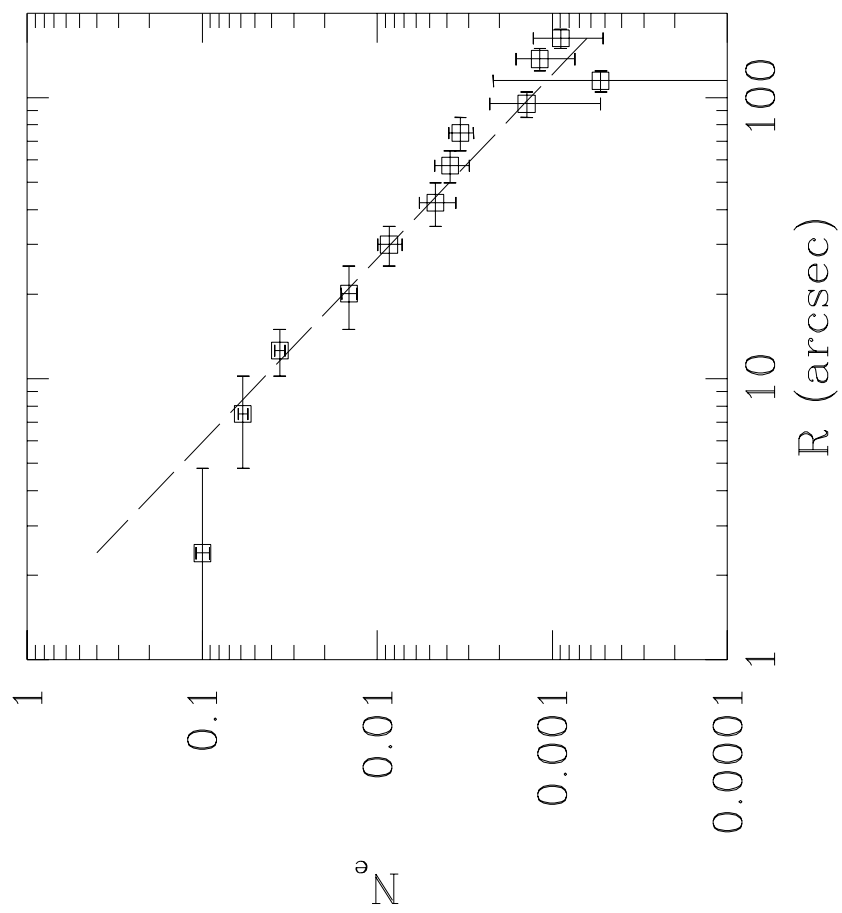
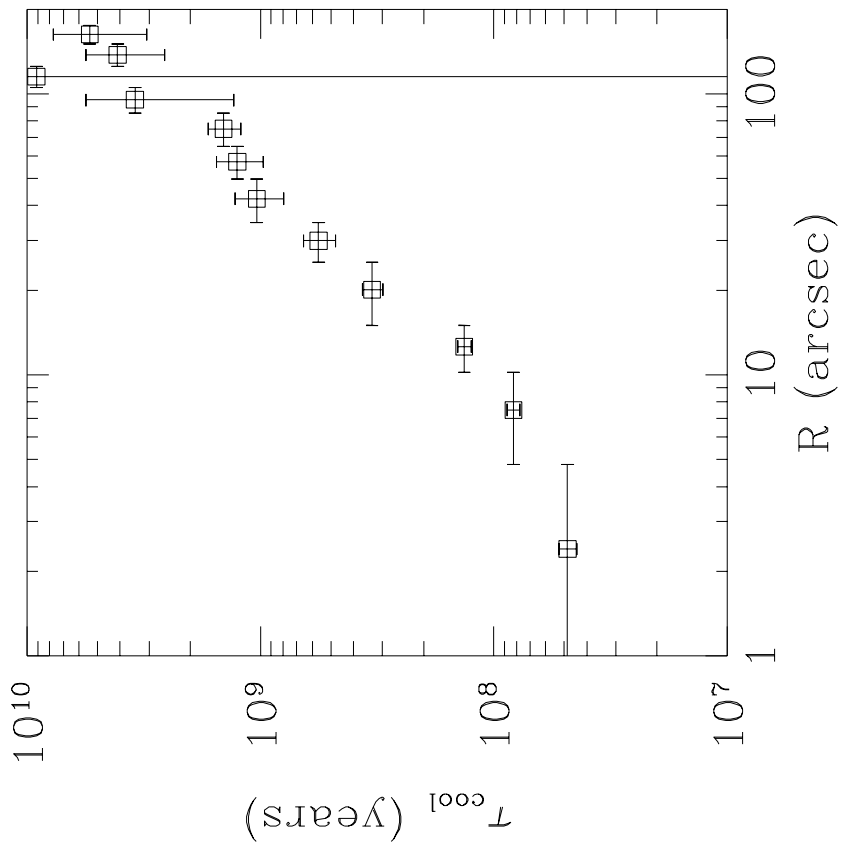


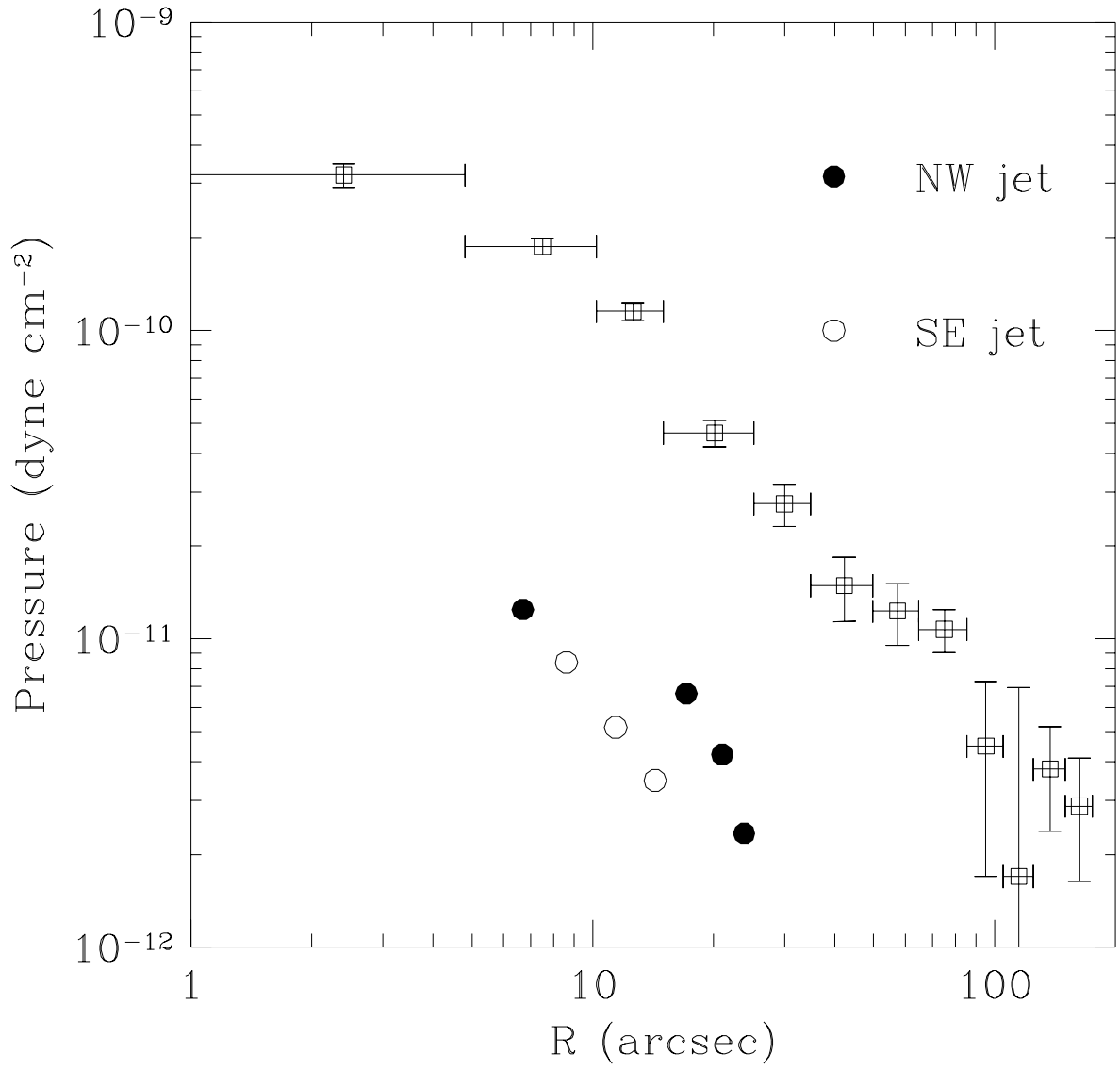


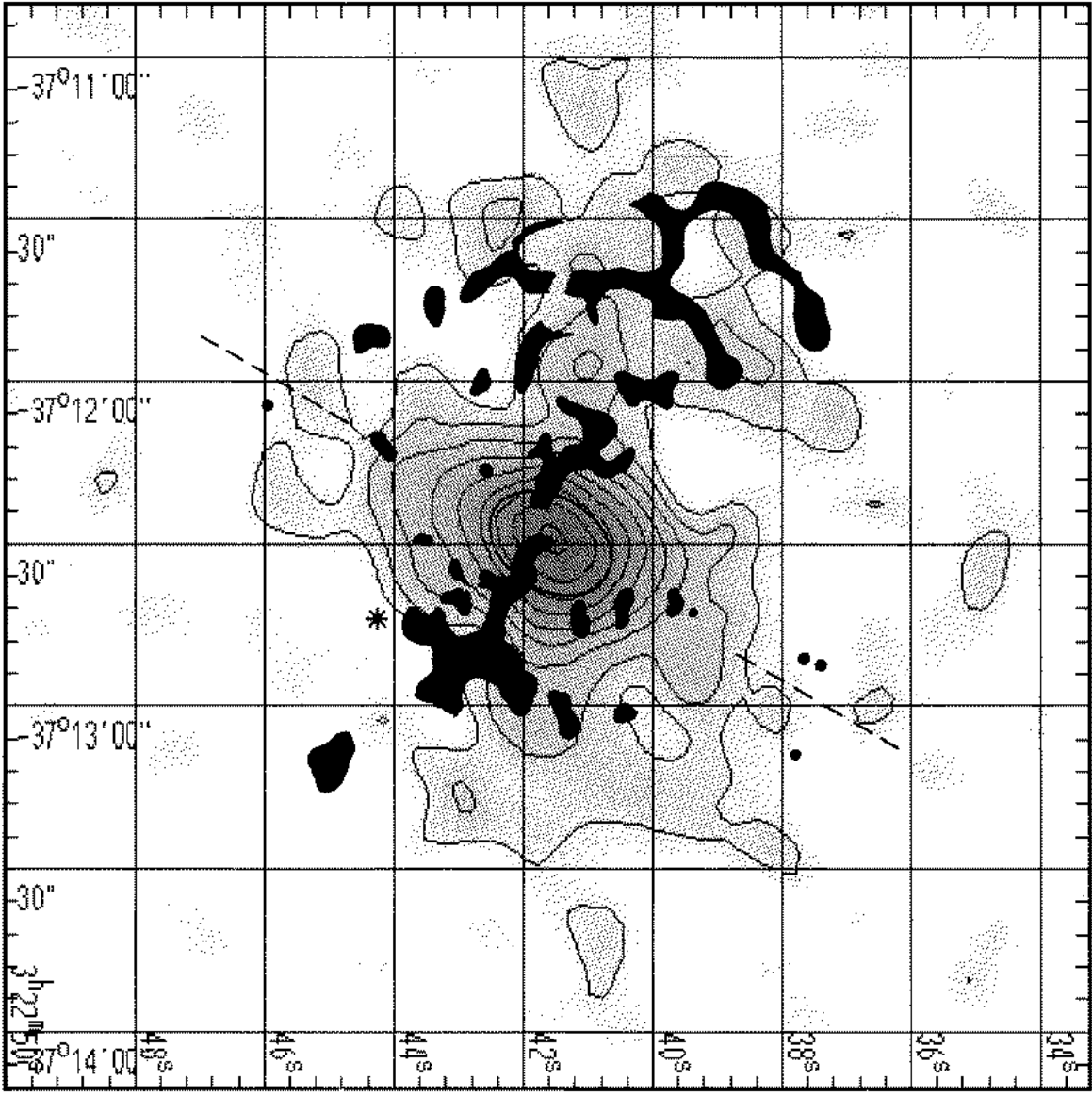


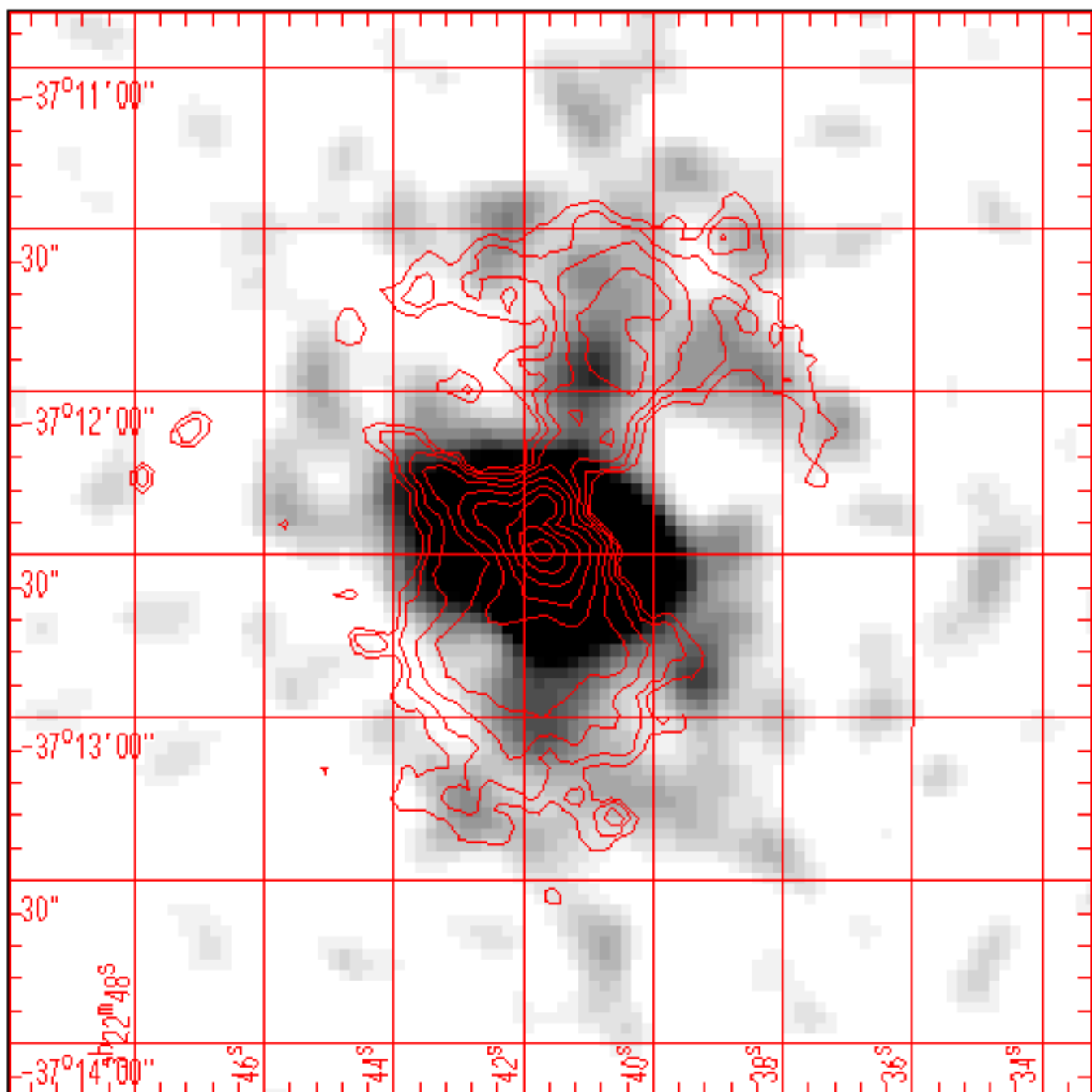


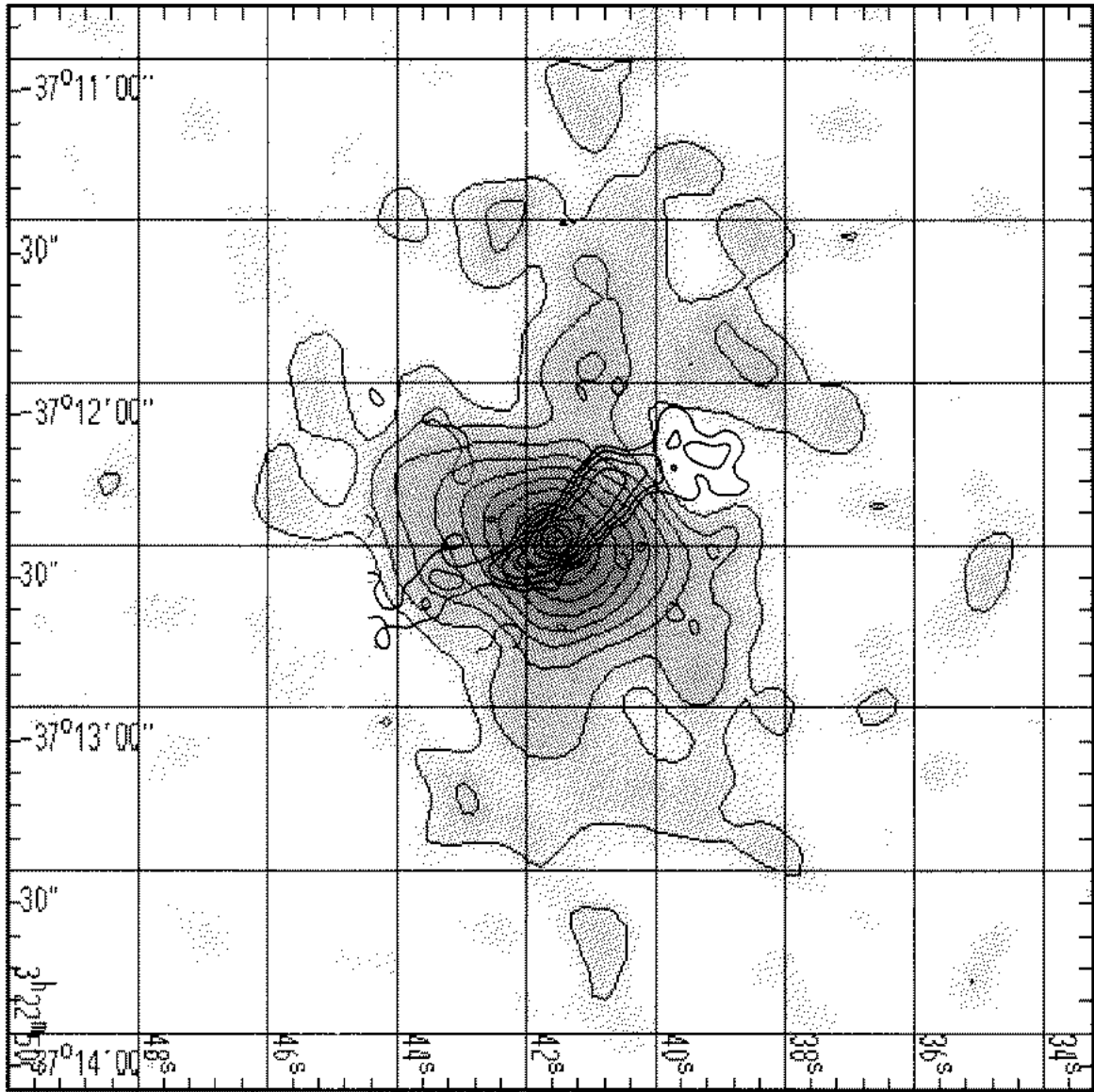












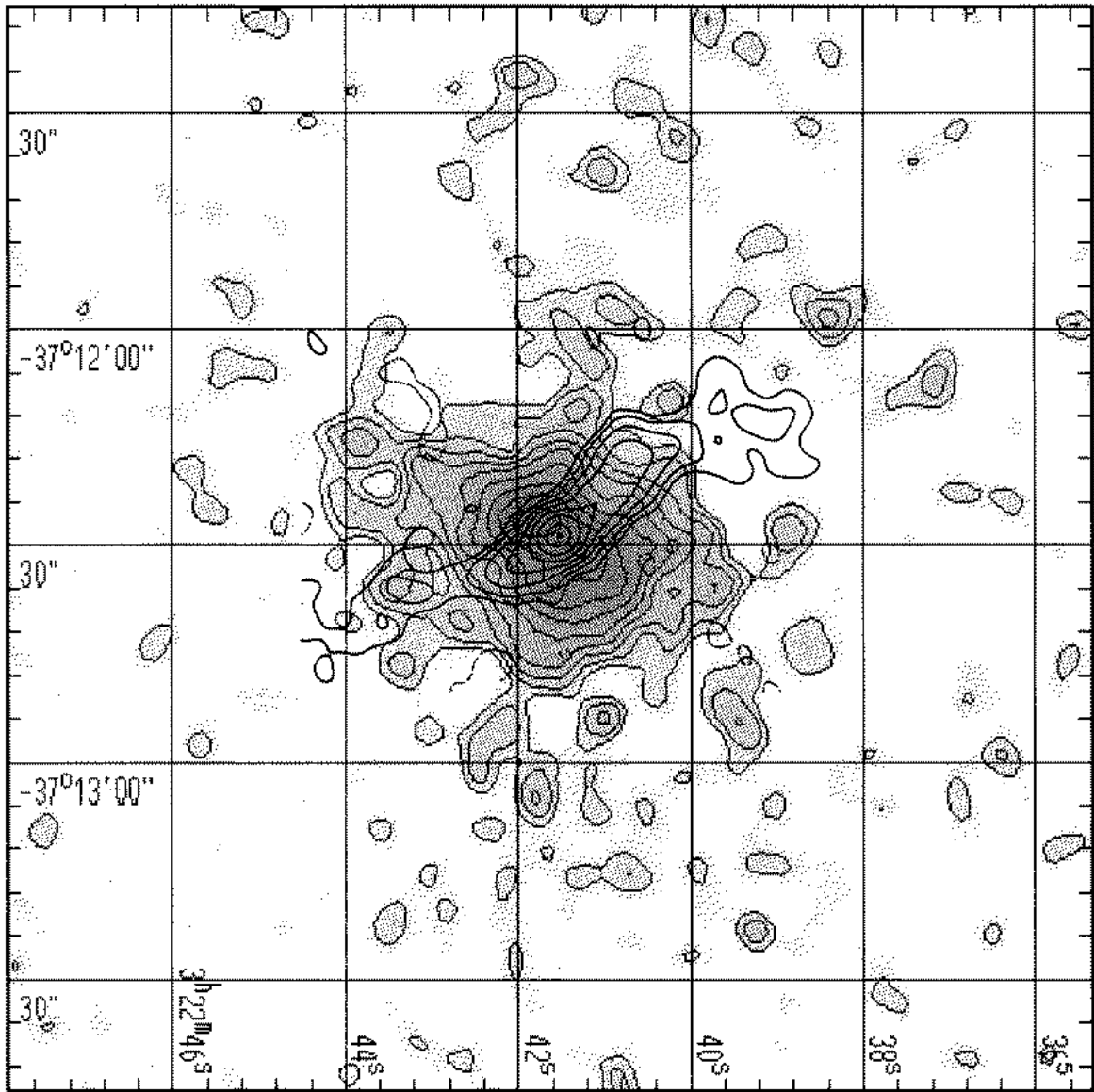


Table 4
SPECTRAL FIT OF PSPC DATA ^a

2-Component fit with solar abundance^b

radius ($''$)	kT ₁ (keV)	kT ₂ (keV)	Norm ^c	χ^2	degrees of freedom
0-60	0.16 (0.13-0.20)	0.83 (0.76-0.90)	1.68 (1.44-1.88)	26.61	23
60-180	0.15 (0.11-0.17)	0.86 (0.72-1.04)	0.74 (0.54-1.03)	17.89	23
0-180	0.16 (0.14-0.17)	0.84 (0.79-0.89)	1.23 (1.08-1.38)	25.34	23

1-component fit with varying abundance^d

radius ($''$)	kT (keV)	Abundance (solar)	χ^2	degrees of freedom
0-60	0.70 (0.65-0.77)	0.12 (0.10-0.15)	14.36	24
60-180	0.59 (0.48-0.70)	0.03 (0.02-0.05)	21.14	24
0-180	0.68 (0.63-0.73)	0.08 (0.06-0.10)	12.99	24

- a. N_H is fixed at the Galactic line-of-sight value, $2 \times 10^{20} \text{ cm}^{-2}$.
- b. Errors are at 90% confidence with 3 interesting parameters.
- c. Normalization of the second component relative to the first component.
- d. Errors are at 90% confidence with 2 interesting parameters.

Table 5
X-RAY FLUX AND LUMINOSITY^a

	Flux ^b	Luminosity ^c
1-component model		
total	$1.9(\pm 0.2) \times 10^{-12}$	$1.7(\pm 0.2) \times 10^{41}$
upper limit of hard binary component	2.9×10^{-13}	2.6×10^{40}
upper limit of nuclear component ^d	1.0×10^{-13}	8.9×10^{39}
2-component model		
total	$2.0(\pm 0.2) \times 10^{-12}$	$1.8(\pm 0.2) \times 10^{41}$
0.2 keV component	$8.1(\pm 1.0) \times 10^{-13}$	$7.2(\pm 0.9) \times 10^{40}$
0.8 keV component	$1.2(\pm 0.1) \times 10^{-12}$	$1.1(\pm 0.1) \times 10^{41}$
upper limit of hard binary component	4.0×10^{-13}	3.6×10^{40}
upper limit of nuclear component ^d	1.0×10^{-13}	8.9×10^{39}

a. The data with $r < 180''$ are used and the errors are based on the acceptable range of normalization at 90%

b. Absorption-corrected flux in unit of $\text{erg sec}^{-1} \text{cm}^{-2}$ in 0.1-2.4 keV.

c. Distance = 27.2Mpc

d. Estimated from the HRI image